

Evaluation of Lateral Resolution of Light Field Cameras

Sowon J. Yoon^{a,b}, Peter Bajcsy^{a,*}, Maritoni Litorja^c, James J. Filliben^a

^aInformation Technology Laboratory, National Institute of Standards and Technology, Gaithersburg, MD, USA, 20899

^bDakota Consulting Inc., Silver Spring, MD, USA, 20910

^cPhysical Measurement Laboratory, National Institute of Standards and Technology, Gaithersburg, MD, USA, 20899

Abstract. Light field cameras are an emerging imaging device for acquiring 3-D information of a scene by capturing a field of light rays traveling in space. As light field cameras become portable, hand-held, and affordable, their potential as a 3-D measurement instrument is growing in many applications, including 3-D evidence imaging in crime scene investigations. We evaluated the lateral resolution of commercially available light field cameras, which is one of the fundamental specifications of imaging instruments. For the evaluation of the camera's lateral resolution, we imaged Siemens stars under various imaging configurations and experimental conditions, including changes in distance between the camera and the resolution target plate, illumination, zoom level, location of the Siemens star in the camera's field-of-view, and cameras of the same model. The analysis results from a full factorial experiment showed that (i) when a lower zoom level of the camera was used, the lateral resolution tended not to be affected by distance; however, when a higher zoom level was used, it tended to decrease significantly with respect to the distance, (ii) the center region of the camera's field-of-view provided a better lateral resolution than the peripheral regions, (iii) a higher zoom level yielded a higher lateral resolution, (iv) the two cameras of the same model used in the study did not show a significant difference in the lateral resolution, and (v) changes in illumination did not affect the lateral resolution of the cameras.

Keywords: light field camera, lateral resolution, Siemens star, modulation transfer function, factorial experiment.

*Peter Bajcsy peter.bajcsy@nist.gov

1 Introduction

Light field cameras, also called plenoptic cameras, capture a field of light rays traveling in space, i.e., the intensity and direction of light rays. This is different from conventional still-picture cameras that acquire the aggregated intensity of incident light rays from all directions. The idea of light field camera was first introduced by Lippmann in 1908,¹ and then realized by Adelson and Wang in 1992.² Since then, various camera configurations to acquire a light field have been proposed: (i) a 2-D array of cameras,³ (ii) a 2-D array of lens-prism pairs in front of the main lens,⁴ and (iii) a 2-D array of microlenses between the imaging sensor and the main lens.⁵

Light field imaging has two major capabilities that differentiate it from the imaging with the traditional cameras: (i) computational photography and (ii) depth estimation. Computational pho-



Fig 1: Light field imaging. (a) A scene observed from multiple viewpoints in a light field camera and (b) the subimages from multiple viewpoints and the camera and image coordinates. Source of the light field image: 4-D Light Field Benchmark.⁷

tography refers to the imaging technology that generates virtual images with artificial camera manipulations, such as viewpoint change, aperture size change, and refocusing, through algorithms after an image is taken.⁶ Depth estimation with a light field camera, on the other hand, is possible since a light field camera is essentially viewed as multiple cameras in a 2-D array (a light field camera with $S \times T$ viewpoints is shown in Fig. 1(a)). The captured light field is represented as $LF(u, v, s, t)$, where (s, t) are the camera coordinates and (u, v) are the image coordinates (see Fig. 1(b)).

One of the fundamental specifications of an imaging system is its lateral (or spatial) resolution to determine the ability of the camera to optically capture fine details in a scene. Lateral resolution of an imaging system broadly refers to the spatial frequency of a pattern (usually line patterns) that the details in the captured image are no longer visually distinguishable.⁸ The contrast of the line patterns in the image generally decreases as the line spacing decreases. Because the perception of low contrasts becomes quite subjective, the lateral resolution is commonly represented as a function of image contrast with respect to spatial frequency, which is called spatial frequency response (SFR) or modulation transfer function (MTF).

ISO 12233 is an international standard for methods for measuring the resolution and the SFR

of electronic still-picture cameras.⁸ According to the 2017 revision, current recommendations for lateral resolution evaluation are (i) slanted-edge analysis and (ii) Siemens star analysis. The slanted-edge method uses a chart with straight edges that have been tilted (see Fig. 2(a)) and looks at the frequency components of the gradient of the edge.⁹ The magnitude of the Fourier transform of the edge gradient is the MTF in this method. If a perfect edge is captured in the image, MTF would be unity at all frequencies. The sharpness is generally decreased when light rays go through lenses and imaging sensor, and high frequency components start to diminish. This method is simple and fast but requires multiple edges at multiple orientations in order to evaluate the angular variations in spatial resolution.

A Siemens star consists of black and white wedges in a circle (see Fig. 2(b)). The lateral resolution is tested by changing the radius of a probe circle whose center is located at the center of a Siemens star. Let N be the number of sectors (black and white wedge pairs) in the Siemens star, and R be the radius of the probe circle in millimeters. The lateral resolution examined by the probe circle with radius r is $\frac{N}{2\pi r}$ lp/mm (line pairs per millimeter). Note that, in this study, the lateral resolution is represented in the object space; that is, the line pairs per millimeter in the scene, not in the camera sensor. The MTF in this method is the image contrast with respect to the spatial frequency, $\frac{N}{2\pi r}$ lp/mm.¹⁰ The implementation of this method is more complicated than slanted-edge analysis, but the lateral resolution can be evaluated in various directions. Both methods are known to exhibit comparable results in lateral resolution evaluation.¹¹

The lateral resolution of various light field cameras was reported in the literature. Firmenich et al.¹⁴ evaluated the lateral resolution of the first generation Lytro camera. A resolution target plate with straight lines was vertically tilted and horizontally rotated from the camera axis, so that the slanted-edge method could be used to evaluate the lateral resolution of the camera, and moreover,

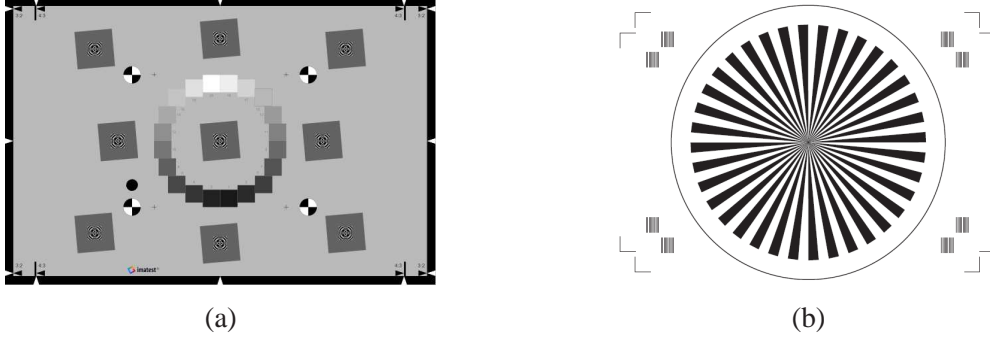


Fig 2: Resolution targets. Examples of (a) slanted-edge chart¹² and (b) Siemens star chart.¹³

the lateral resolution of a focused light field camera¹⁵ could be assessed, which gives an enhanced lateral resolution. Fu et al.¹⁶ compared the lateral resolutions of a conventional camera and a light field camera (by placing a microlens array in front of the main lens), and found that (i) the conventional camera has a higher lateral resolution at the focal plane than the light field camera, but (ii) the light field camera has a wider depth of field than the conventional camera. Another study by Damghanian et al.¹⁷ conducted the lateral resolution evaluation from a sampling pattern cube (SPC) model on the data collected by the Raytrix R29 camera.¹⁸ They found that (i) the camera was capable of achieving the lateral resolution of approximately a quarter of 0.5 cycles/pixel at the distance of 800 mm with refocused images, and (ii) the results from the SPC model showed agreement with the empirical results.

In this paper, a comprehensive lateral resolution evaluation of the Lytro Illum cameras,¹⁹ which are commercially available, is reported. The resolution target plate has an array of 3×3 Siemens stars to measure the lateral resolution at different locations in the field-of-view of the camera. The light field images of the resolution target were collected to conduct a full factorial experiment with the following variables (factors):²⁰ (i) distance between the camera and the target, D , (ii) camera, C , (iii) zoom level, Z , (iv) Siemens star location in the camera's field-of-view, L , and (v) illumination, I . Under each condition, five images were collected—local replicates—to observe the effect

of random noise, for example, from the imaging sensor or the lamps. The entire data collection was repeated three times—global replicates, R —to observe any systematic errors coming from device setup and operation of the experiments. The contributions of this paper are:

- Design of a full factorial experiment for a comprehensive lateral resolution evaluation of a commercial light field camera
- Collection of light field data and development of an automatic algorithm for Siemens star analysis
- Statistical analysis of the factors that affect the lateral resolution
- Design of an interactive web-based system for browsing the collected images and viewing the results from the lateral resolution evaluation.

1.1 Scope

This study was conducted under the scenario that the light field camera was used in crime scene investigations. Light field cameras are of interest to the forensic community because the operation of light field cameras is as simple as that of conventional cameras and they are affordable for most forensic laboratories. Three-dimensional forensic evidence such as tire tread and shoe imprints in substances like mud or snow can provide useful information to potentially help link a suspect to a crime scene. The accuracy of 3-D details obtained from imaging systems and their lateral and depth resolutions are very important in forensic investigations when the evidence collected from a crime scene is compared to the reference from a suspect. For example, if a trace of shoeprints was found in a crime scene, not only the size and sole pattern of a shoe are important pieces of information to examine the linkage between a suspect and the crime scene, but the distinctive wear and tear found

in a shoe that belongs to a particular individual is also critical in comparison.^{21,22} The experimental setup in this paper is therefore adapted to a forensic scenario; the distance between the camera and the target is within 1 m, and the zoom levels are set to fit an entire or a partial shoeprint in the camera's field-of-view. However, the methodology for the lateral resolution evaluation and statistical analysis presented in this paper is general and can be used for any data collected using any camera for the same purpose.

2 Evaluation of Lateral Resolution of a Light Field Camera

Lateral resolution of a camera is typically evaluated by collecting the images of a resolution target and analyzing the sharpness of the images of the resolution target. In this study, we use the Siemens stars as a resolution target and develop an algorithm to automatically detect the Siemens stars from the collected images, extract the MTF, and estimate the lateral resolution corresponding to a desirable image contrast level.

2.1 Resolution Target

Two resolution target plates were used in this study to evaluate the lateral resolution at two different zoom levels. Each plate contains an array of 3×3 Siemens stars, but the size of the Siemens stars is different between the two plates. The Siemens stars in one plate have the radius of 20.743 mm for a low zoom level of the camera, and those in the other plate have the radius of 14.393 mm for a high zoom level. At each zoom level, the camera's zoom factor is set such that the nine Siemens stars tightly fill the field-of-view at any distance (see Fig. 3(a)). This way, if the lateral resolution is affected by lens distortion (lens distortion is generally more severe on the fringe of the lens than at its center) or lens defect, it can be detected.¹⁰ The number of black and white wedge pairs in

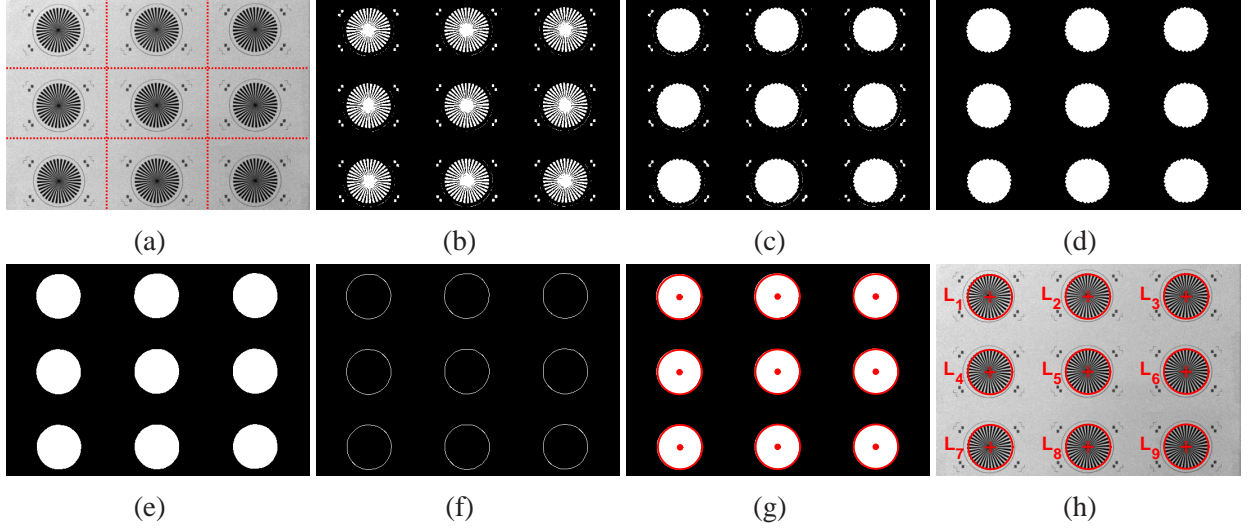


Fig 3: Siemens star detection. (a) A lateral resolution target consisting of 3×3 Siemens stars, (b) binarization, (c) morphological close operation, (d) finding nine largest connected components, (e) finding convex hulls, (f) finding Siemens star edges, (g) fitting a circle to the edge of each Siemens star, and (h) the detection result of the Siemens stars.

a Siemens star is 36 ($N = 36$). The resolution targets were printed on 100 lb silk paper using a Ricoh Pro7100 printer²³ at 600 dpi.

2.2 Siemens Star Detection

Images taken from a light field camera go through a decoding process, which converts a raw light field image in 2-D to 4-D (or 5-D in the case of a color image) light field data, $LF(u, v, s, t)$. After decoding the light field, the subimage from the center viewpoint, $I_0(u, v) = LF(u, v, s_0, t_0)$, where (s_0, t_0) is the center camera location in the camera coordinates (see Fig. 1(b)), is examined for lateral resolution evaluation. The Siemens stars in the image are detected by fitting a circle to the outer edge of each Siemens star. The detailed procedure for Siemens star detection is below with an example shown in Fig. 3.

1. Convert the color image $((R(u, v), G(u, v), B(u, v)))$ to a grayscale image $(I(u, v))$ by following ITU-R Recommendation BT.601:²⁴ $I(u, v) = 0.2989 R(u, v) + 0.5870 G(u, v) +$

$$0.1140 B(u, v).$$

2. Divide the image into 3×3 sections equally along width and height (see Fig. 3(a)).
3. Binarize each of nine subregions using Otsu's method²⁵ (see Fig. 3(b)). Binarizing the subregions individually copes with the uneven illumination over the resolution target plate.
4. Perform a morphological close operation to connect the wedges in the Siemens stars (see Fig. 3(c)).
5. Find the nine largest connected components in the entire image (see Fig. 3(d)).
6. Find the convex hull of each connected component (see Fig. 3(e)).
7. Find the outer edge of each convex hull (see Fig. 3(f)).
8. Fit a circle to the edge points of each Siemens star²⁶ (see Fig. 3(g)).

The detected Siemens stars are labeled as $\{L_1, L_2, \dots, L_9\}$ (from left to right and from top to bottom), as shown in Fig. 3(h).

2.3 Modulation Transfer Function

For each Siemens star, the image intensity profile is examined along a probe circle. The center of the probe circle is the center of the Siemens star, and its radius changes from 1 pixel to the radius of the Siemens star with a step size of 0.5 pixels (see Fig. 4(a)). At each radius value, the image intensity values are sampled along the probe circle with an angular step size of $\frac{2\pi}{144}$ which allows two sampling points from each wedge in a Siemens star. Examples of the image profiles at various radius values of a probe circle (color-coded in Fig. 4(a)) are shown in Fig. 4(b). It is observed that

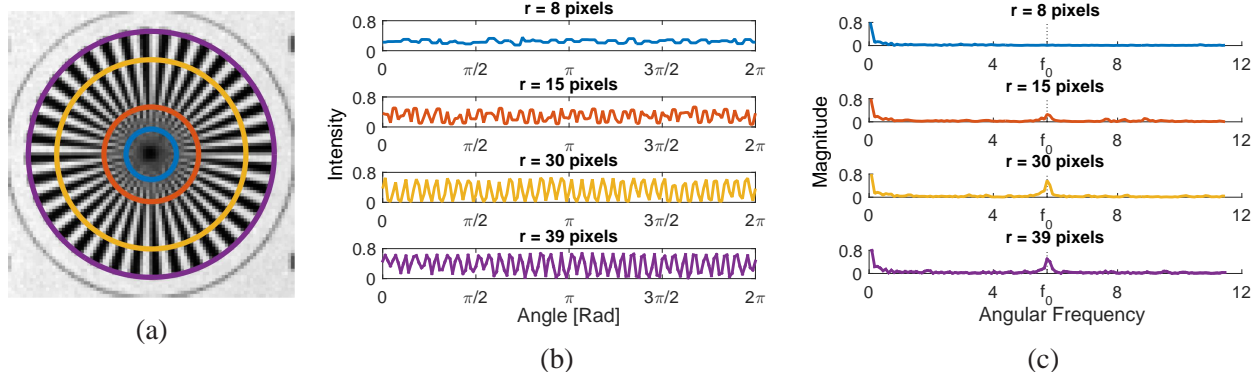


Fig 4: Example of image profile variations as the radius of probe circle changes (8, 15, 30, and 39 pixels). (a) A Siemens star, (b) image intensity profiles along each of the four probe circles, and (c) Fourier transform of the image intensity profiles.

the image profile gradually shows a greater image contrast between black and white wedges as the radius of the probe circle increases.

For each image profile, a Fourier transform is performed, and we look at the magnitude at the angular frequency of the Siemens star, that is, $f_0 = \frac{N}{2\pi}$, where N is the number of black and white wedge pairs in a Siemens star (see Fig. 4(c)). In order to correspond to image contrast, the magnitude in MTF is defined as the doubled amplitude in Fourier transform. The MTF of an image from a Siemens star is then normalized by the largest magnitude found in that image, which yields the maximum magnitude of a normalized MTF is always 1. The spatial frequency, f [lp/mm], associated with a probe circle with the radius of r [mm] is as follows:

$$f = \frac{N}{2\pi r}. \quad (1)$$

The spatial frequency associated with a probe circle and the magnitude of the Fourier transform of the image intensity profile along the probe circle yields a data point in MTF for a Siemens star, as shown in Fig. 5.

The lateral resolution in this paper is defined as the spatial frequency corresponding to MTF_{10} ,

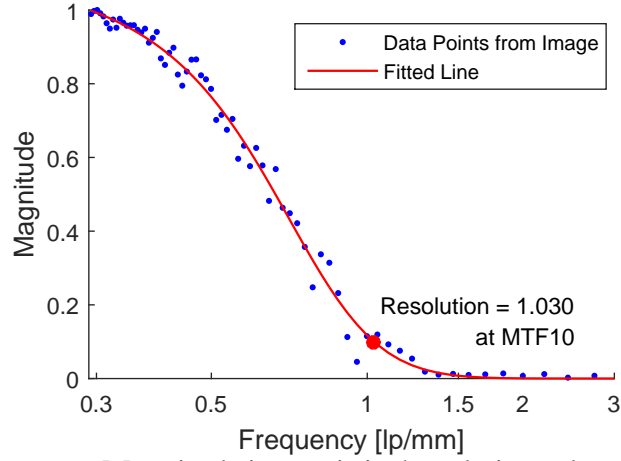


Fig 5: MTF of a Siemens star. Magnitude in y-axis is the relative value to the maximum magnitude observed in the Siemens star. Notice that the x-axis is on a log scale.

where the magnitude of Fourier transform of an image profile is 10% of the largest magnitude found in the Siemens star. In order to estimate the lateral resolution corresponding to MTF_{10} , the following model is fit to the data points in MTF using the Levenberg-Marquardt algorithm:

$$m = \frac{1}{a + be^{cf}} \quad (2)$$

where m is the magnitude of Fourier transform of an image profile and f is the spatial frequency. The goodness-of-fit was evaluated by the pooled residual standard deviation. The residual standard deviation for an MTF plot is defined as follows:

$$STD_k^{res} = \sqrt{\frac{\sum_{i=1}^{n_k} [g_k(f_i) - m_i]^2}{n_k - p}} \quad (3)$$

where $g_k(\cdot)$ is the fitted model of the k 'th MTF plot with n_k data points and p is the degrees of

freedom ($p = 3$). The pooled residual standard deviation is then calculated by

$$STD^{pooled} = \sqrt{\frac{\sum_{k=1}^K (n_k - 1) STD_k^{res}}{\sum_{k=1}^K n_k - K}} \quad (4)$$

where K is the total number of MTFs. We found $STD^{pooled} = 0.0189$, which indicates about 1.9% error between the data points and the estimates.

Given a desirable magnitude value m (in this paper, $m = 0.1$), the corresponding lateral resolution f_L can be found as follows:

$$f_L = \frac{1}{c} \log \left[\frac{1}{b} \left(\frac{1}{m} - a \right) \right]. \quad (5)$$

Figure 5 shows the fitted model along with the estimated lateral resolution at MTF_{10} for a Siemens star.

3 Experimental Setup

The data collection for this lateral resolution evaluation was conducted under various imaging conditions, including changes in distance between the camera and the resolution target plate (15 levels), the camera used for image acquisition (two cameras from the same model), illumination (2 levels), zoom (2 levels), and location of Siemens stars in the resolution target plates (9 locations). Under each condition, five images were collected to examine random noise coming from the imaging sensor or the light sources (local replicates). When a camera was switched to the other one, the camera was aligned to the resolution target plate such that the camera moved perpendicular to the resolution target plate. The entire data collection was repeated three times to observe any systematic errors during the image collection (global replicates).

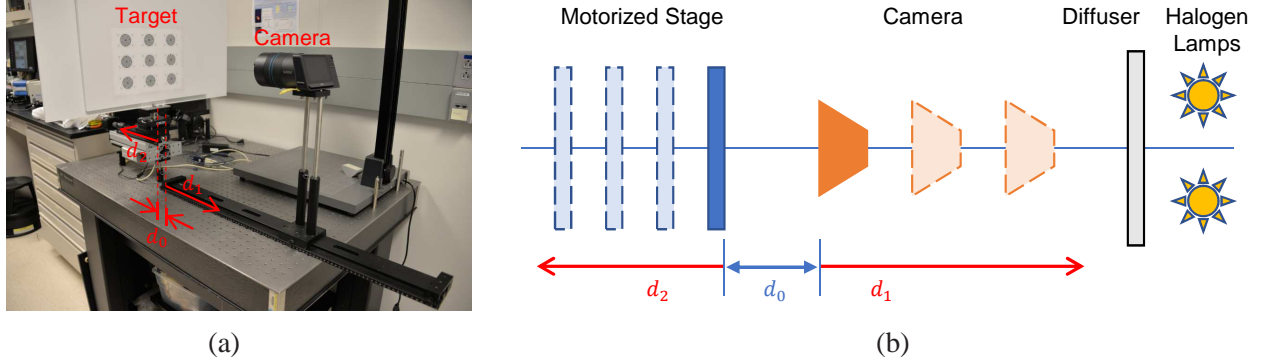


Fig 6: Camera setup. (a) Photograph of the camera system for data collection and (b) diagram of the camera, resolution target, and illumination.

3.1 Camera System Configuration

The camera system consists of (i) a light field camera mounted on a rail stand with a ruler, and (ii) a resolution target plate attached to a motorized stage (see Fig. 6). The camera stand on the rail moves manually, and the distance from the origin of the rail system is denoted as d_1 . The motorized stage for the resolution target plate, on the other hand, is controlled automatically with a precision of 10 240 steps in 1 mm. The motorized stage moves in the opposite direction to the camera, and the distance from the origin of the motorized stage is denoted as d_2 . The distance between the origins of the rail and the motorized stage is $d_0 = 80$ mm.

The data collection was automated by the following control interfaces: LabVIEW²⁷ to operate the motorized stage for the resolution target plate and Lytro Power Tools Beta 1.0¹⁹ to set the camera parameters and capture the images, and the procedure was interrupted when the camera location needed to be changed. The following settings were used for both cameras:

- Zoom and focus rings locked: The zoom and focus of the cameras were controlled only by commands, not by rotating the rings manually. The predetermined zoom and focus steps of the cameras with respect to distance were used (see Section 3.4).
- Auto-focus disabled

Table 1: Variables considered in the lateral resolution evaluation of light field cameras.

Factor	Description	Labels	Values
Distance (D)	Distance between camera and resolution target plate [mm]	$\{D_1, D_2, \dots, D_{15}\}$	$\{330, 380, \dots, 1030\}$
Camera (C)	Cameras from the same model	$\{C_1, C_2\}$	$\{\text{Camera 1, Camera 2}\}$
Zoom (Z)	Size of resolution target plate fitting the entire field-of-view [mm]	$\{Z_1, Z_2\}$	$\{280 \times 215, 195 \times 125\}$
Location (L)	Location of the Siemens stars on the resolution target plate	$\{L_1, L_2, \dots, L_9\}$	$\{\text{Top left, Top middle, \dots, Bottom right}\}$
Illumination (I)	Lighting condition	$\{I_1, I_2\}$	$\{\text{Ambient, Halogen}\}$

† 3 global replicates (R) ‡ 5 local replicates

- Auto white balance: The color temperature and tint were chosen automatically by the camera.
- Programmed exposure mode: The ISO and shutter speed were set by the camera based on metered value and exposure value compensation value.

Two light stands were placed behind the camera. A halogen lamp in a soft box with a diffuser was mounted on each light stand, and a drape-type diffuser was installed between the camera and the light sources for more effective illumination diffusion.

3.2 Variables

The dataset for the lateral resolution evaluation of the light field cameras was collected with the following variables: (i) distance between camera and resolution target plate, (ii) camera, (iii) zoom level, (iv) location of the Siemens stars in the camera’s field of view, and (v) illumination. Table 1 summarizes the variables considered in the study.

Distance The distance between camera and resolution target plate is defined as $D = d_1 + d_2 + d_0$, and it ranges from 330 mm to 1030 mm with a step size of 50 mm, yielding 15 levels. The camera

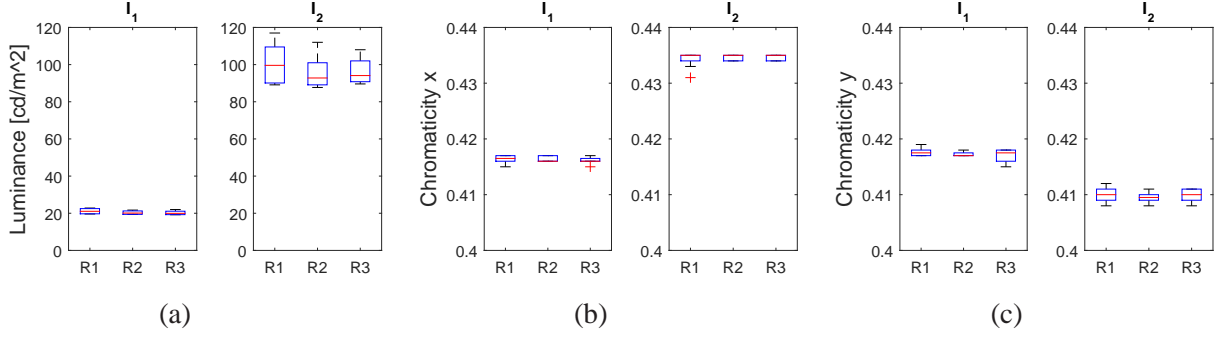


Fig 7: Box plots of illumination measurements under conditions of (R, I) . (a) Luminance Y , (b) chromaticity x , and (c) chromaticity y .

and resolution target plate distance from their respective origins, (d_1, d_2) , are $\{(250, 0), (250, 50), (250, 100), (250, 150), (400, 50), (400, 100), (400, 150), (550, 50), (550, 100), (550, 150), (700, 50), (700, 100), (700, 150), (800, 100), (800, 150)\}$ mm.

Camera The light field cameras used in this study, C , are two Lytro Illum cameras.¹⁹ The cameras were purchased at two different time points (~ 2 years apart), and we found that the offset and orientation of the microlens arrays in the two cameras are slightly different.

Zoom The two levels of zoom, Z , were selected to examine the situation where the cameras were used to obtain 3-D shoeprint evidence. At the zoom level of Z_1 , the resolution target plate in the size of $280 \text{ mm} \times 215 \text{ mm}$ (with the Siemens stars with the radius of 20.743 mm) fills the entire field-of-view of the cameras at any distance; at the zoom level of Z_2 , the resolution target plate in the size of $195 \text{ mm} \times 125 \text{ mm}$ (with the Siemens stars with the radius of 14.393 mm) fills the camera's field-of-view.

Location Each resolution target plate has nine Siemens stars, and they are labeled as $\{L_1, L_2, \dots, L_9\}$ (from left to right and from top to bottom), as shown in Fig. 3(h).

Illumination The default illumination condition for the data collection (I_1) was the ambient lighting in an office-like environment. Additional halogen lamps with diffuser (I_2) were used to see the impact of illumination change on lateral resolution of the cameras. The illumination was

measured every time the condition changed using Konica Minolta CS-100 Chroma Meter.²⁸ The distribution of the luminance Y [cd/m²] and chromaticity x and y is shown in Fig. 7. Luminance is higher when I_2 than when I_1 , and the color distributions are also different depending on the condition of I . The distributions, however, are consistent across R .

3.3 Camera Alignment

To ensure the camera axis was perpendicular to the resolution target plate during the data collection, a camera alignment was conducted every time a camera was mounted. A cross-hair laser module was attached to the camera on top of the main lens approximately parallel to the camera axis, and the point where the laser intersects the resolution target plate was observed while the camera moved back and forth along the rail and the resolution target plate also moved back and forth. The pan and tilt of the camera on the mount were adjusted until the laser point on the target plane stayed still as the distance between the camera and the resolution target plate changed.

3.4 Zoom and Focus Presets

The zoom and focus steps of the main lens of the cameras were predetermined at every D . The zoom and focus steps of a Lytro Illum camera range from 1 to 1522 with a step size of 1. At a distance point, a set of images of the resolution target was collected by changing the zoom step by 1, and the autofocus function in the camera was used to adjust the focus lens of the cameras. The radius of the nine Siemens stars on the resolution target plate was estimated and plotted in Fig. 8. Then, the optimal zoom step for a distance point was chosen as the one where the median radius of the Siemens stars on a resolution target plate was the closest to 40 pixels.

Once the zoom steps were determined at every D , the optimal focus step for (D, Z) was deter-

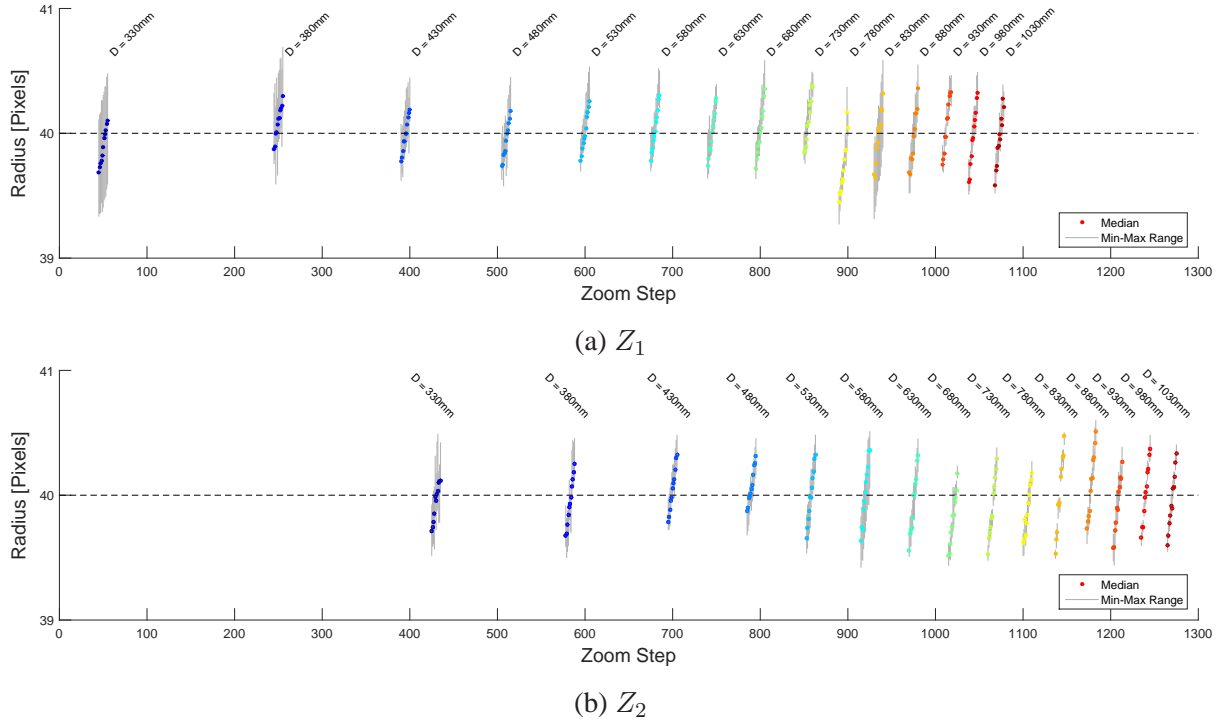


Fig 8: Selection of zoom steps of the camera with respect to D for (a) Z_1 and (b) Z_2 . Gray bars represent the range of radius of Siemens stars on a resolution target plate at (D, Z) , and circles represent the median value of the radius.

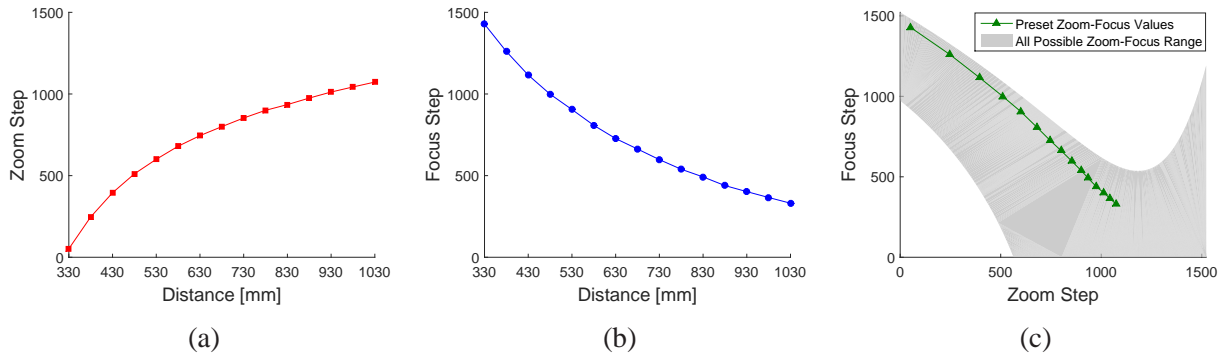


Fig 9: Zoom and focus steps set at every distance point when Z_1 . (a) Preset zoom step at each distance point, (b) preset focus step at each distance point, and (c) preset zoom and focus steps used in the study overlaying all possible zoom-focus step pairs.

mined by collecting five images with autofocus. The focus step with a majority vote was chosen.

The zoom and focus steps that were used in this study are shown in Figs. 9 and 10.

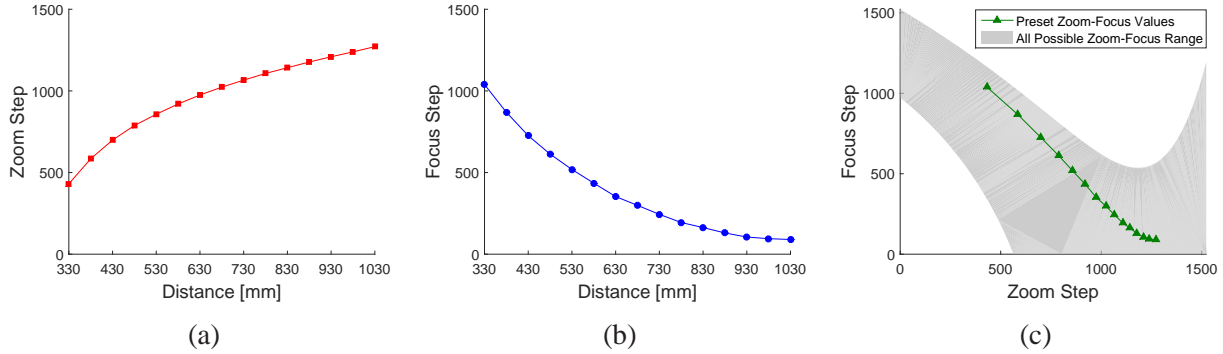


Fig 10: Zoom and focus steps set at every distance point when Z_2 . (a) Preset zoom step at each distance point, (b) preset focus step at each distance point, and (c) preset zoom and focus steps used in the study overlaying all possible zoom-focus step pairs.

4 Experimental Results

A dataset of light field images for lateral resolution evaluation was collected to conduct a full factorial experiment with the six variables, (R, C, Z, I, D, L) . The images were examined to ensure that the size of the Siemens stars was the same at any distance and zoom levels. In this section, we report the variables that affect the lateral resolution significantly and present the mean trend of the lateral resolution when the level of the variables changes.

4.1 Dataset

Data collection was conducted under conditions with four variables (D with 15 levels, C with 2 levels, Z with 2 levels, and I with 2 levels), and five local replicates and three global replicates were made. This yielded 1800 light field images (a total size of 99.75 GB). Raw light field images were decoded using the software provided by the camera manufacturer (Lytro Power Tools Beta 1.0¹⁹). The decoded light field data from a raw image is in $14 (S) \times 14 (T) \times 541 (U) \times 376 (V) \times 3 (Channels)$.

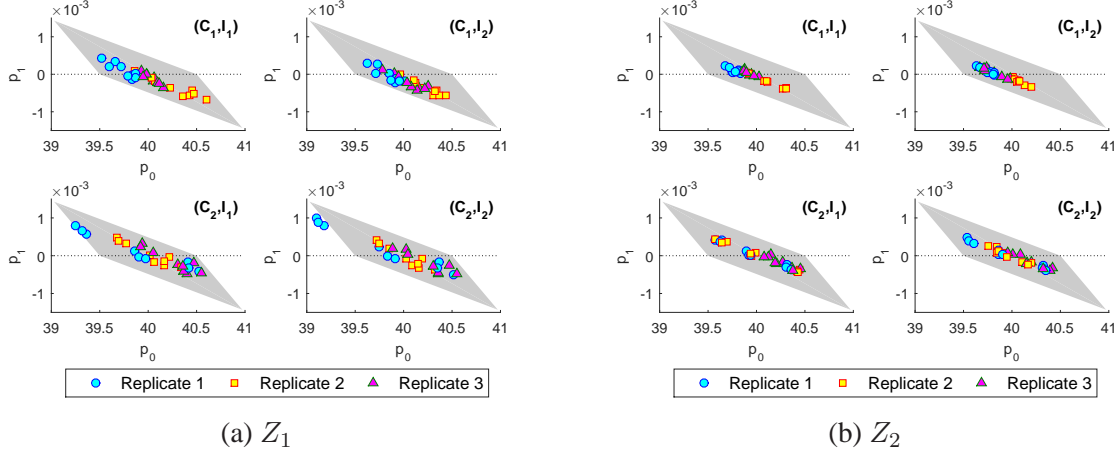


Fig 11: Parameters of linear model fit to the radius of Siemens stars with respect to distance D when (a) Z_1 and (b) Z_2 . Parameters (p_0, p_1) are within the gray region when the radius of Siemens star is 40 ± 0.5 pixels in the images collected while D changes between 330 mm and 1030 mm.

4.2 Verification of Zoom Constraint

Each zoom level was set to keep the size of the Siemens stars the same in the images collected under all conditions. To verify if the constraint was satisfied during the data collection, a linear model was fit to the radius of the Siemens star (r) with respect to D for a given (R, C, Z, I) :

$$r = p_1 D + p_0 \quad (6)$$

where p_1 and p_0 are the slope and the intercept of the linear model, respectively. If the zoom and focus lenses were well adjusted while D changed, the radius of the Siemens star would be consistent, hence, the slope of the linear model p_1 would be ideally 0. If we allow the radius variations within ± 0.5 pixels from the expected radius of 40 pixels, a set of parameters (p_0, p_1) satisfying this acceptable error bound would reside within the gray region in Fig. 11. We observed that most of data points were within the acceptable error bound.

However, three data points were slightly off from the acceptable error bound. The error cases came from the Siemens stars (L_1, L_4, L_7) in the images collected under the condition (R_1, C_2, Z_1, I_2) .

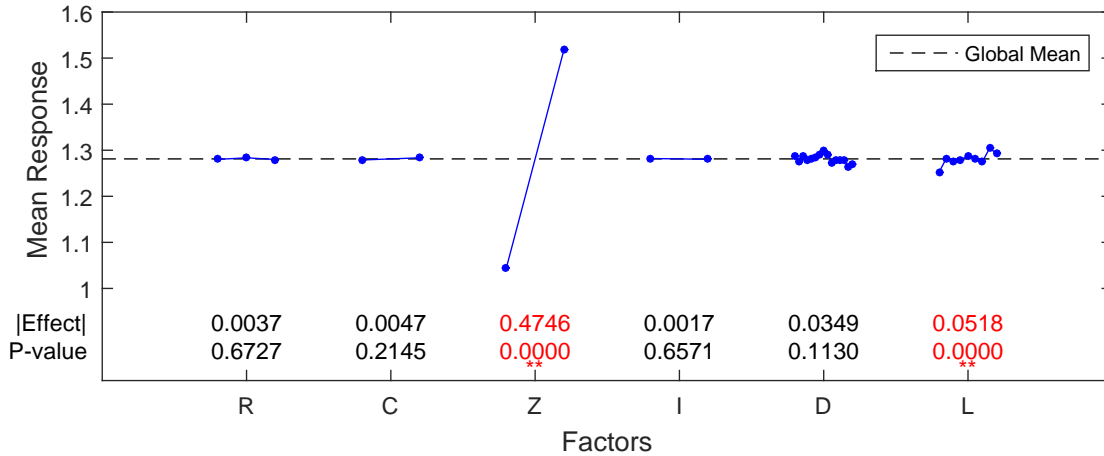


Fig 12: Main effects of the full factorial experiment along with the p -values from F -tests for each factor. The factors for which the null hypothesis ($H_0 : \mu_1 = \mu_2 = \dots = \mu_l$) is rejected at a significance level of 0.01 are highlighted with a red color and double asterisks.

These Siemens stars are located on the left column of the 3×3 array of the Siemens stars. All these cases show a positive slope, which means the radius of the Siemens stars tends to increase as the distance increases. Nevertheless, this constraint violation on the three data points was not considered as a serious error because the violation was not severe, and thus, no data points were excluded from the lateral resolution evaluation.

4.3 Evaluation of Lateral Resolution of Light Field Cameras

In Section 4.3.1, a full factorial experiment with the six variables (R, C, Z, I, D, L) determines the factors that have a significant impact on the camera's lateral resolution. Then, the mean trend of the lateral resolution under conditions defined by the significant factors is presented in Section 4.3.2.

4.3.1 Factors That Affect Lateral Resolution

A full factorial design is to run experiments with all possible combinations of the levels from variables. Main effects and interaction effects are calculated from the data collected under the factorial

Table 2: Ranked main effects and two-factor interactions according to the absolute magnitude of the effect for Z_1 .

Factor	Effect	Factor	Effect
L	0.0453	(C,D)	0.0051
D	0.0245	(R,L)	0.0043
(D,L)	-0.0172	(R,I)	-0.0037
R	0.0107	I	0.0023
(I,D)	0.0099	(R,D)	-0.0020
(R,C)	0.0079	(C,L)	-0.0012
(I,L)	-0.0075	(C,I)	-0.0006
C	0.0057		

design.²⁰ The main effect of a variable is the average impact of the variable on the responses over all possible conditions of the other variables. For a variable with two levels, its main effect is the difference in average value of the responses between the data points belonging to level 1 and the data points belonging to level 2. For a variable with more than two levels, we chose two levels that gave the maximum and the minimum of the average responses and treated as a variable with two levels. For each variable, one-way ANOVA (Analysis of Variance) was conducted to test the null hypothesis H_0 that the means of all the levels are the same (i.e., $H_0 : \mu_1 = \mu_2 = \dots = \mu_l$, where l is the number of levels for the variable). The response in the analysis was the lateral resolution corresponding to MTF_{10} .

Figure 12 shows the main effects of the six variables along with the p -value from an F -test for each variable. Two variables, Z and L , have a significant impact on the lateral resolution, whereas D , C , R , and I barely affect the lateral resolution at a significance level of 0.01. For the variable L which has more than two levels, Tukey's test was conducted to compare the pairs of means from different levels. Two clusters of the levels in L were found: central region ($\{L_2, L_4, L_5, L_6, L_8, L_9\}$) and peripheral region ($\{L_1, L_3, L_7\}$).

Table 3: Ranked main effects and two-factor interactions according to the absolute magnitude of the effect for Z_2 .

Factor	Effect	Factor	Effect
L	0.0583	R	0.0068
D	0.0573	I	0.0056
(D,L)	-0.0307	C	0.0037
(R,D)	-0.0089	(C,D)	0.0027
(R,C)	-0.0088	(R,L)	-0.0022
(I,D)	-0.0082	(R,I)	-0.0018
(I,L)	-0.0076	(C,I)	-0.0011
(C,L)	-0.0071		

We also looked at the two-factor interactions of the variables. When any two variables do not behave additively, a two-factor interaction exists between them, and they should be considered jointly in the analysis.²⁰ Since the effect of the variable Z overwhelms the responses, two-factor interactions of the five other variables are calculated under each level of Z . Tables 2 and 3 show the the main effects and two-factor interaction effects that are ordered according to their magnitude under Z_1 and Z_2 separately. A couple of noteworthy observations are as follows:

- L has the most significant impact on the lateral resolution, which is followed by D and the interaction between D and L .
- The impact of D is comparable to L when Z_2 , whereas it is about a half of the impact of L when Z_1 .
- R , C , and I have little impact on the lateral resolution.

Since the impact of D on lateral resolution is as big as that of L when Z_2 , we consider D as one of the significant factors along with Z and L in the following analysis.

4.3.2 Mean Trend of Lateral Resolution

With the analysis results from Section 4.3.1, the three most influential variables— Z , L , and D —are considered for evaluating the mean trend of the lateral resolution of the light field cameras. For each condition of Z , the following second-order polynomial model was fit to the data:

$$f_L(D, L_x, L_y; Z) = a_0 + a_1 D + a_2 L_x + a_3 L_y + a_4 D^2 + a_5 L_x^2 + a_6 L_y^2 + a_7 D L_x + a_8 D L_y + a_9 L_x L_y \quad (7)$$

where (L_x, L_y) is the location of L relative to L_5 (the Siemens star at the center of the resolution target plate). STD^{res} are 0.0349 lp/mm for Z_1 and 0.0408 lp/mm for Z_2 ; STD^{pooled} is 0.0379 lp/mm. Figure 13 shows the mean lateral resolution with respect to D , and Fig. 14 shows the mean lateral resolution with respect to L .

The minimum resolvable distance, d_L , refers to the minimum distance between scene objects that can be distinguished in an image from a camera system. The minimum resolvable distance can be derived from the lateral resolution of the camera system f_L as follows:

$$d_L = \frac{1}{2f_L}. \quad (8)$$

Table 4 shows the minimum resolvable distance of the light field cameras that were studied in this paper. As the lateral resolution is a function of D and L under the conditions of Z , the range of the minimum and maximum values is reported.

Based on the experimental results for the lateral resolution evaluation of the light field cameras, we can draw the following inferences about the lateral resolution measurements and the variables.

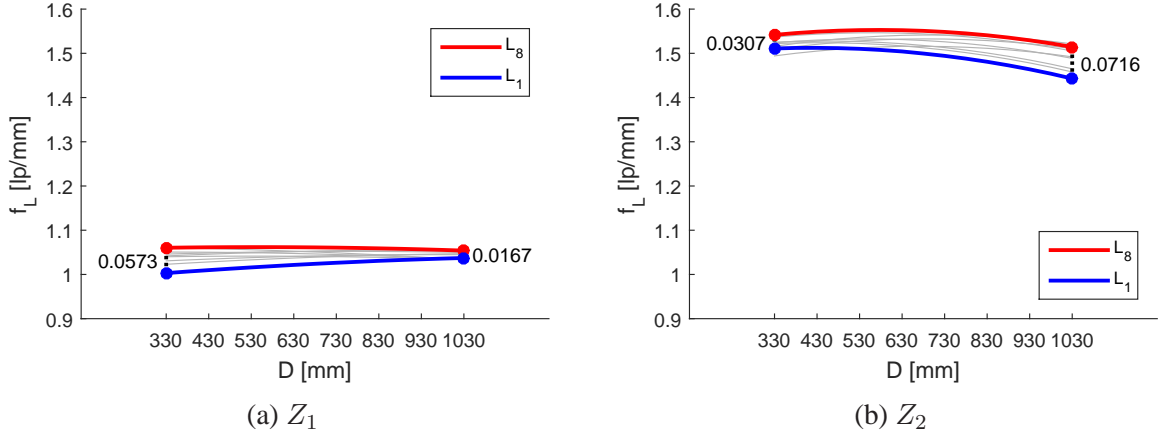


Fig 13: Mean lateral resolution with respect to distance D under the conditions of Z at $MTF10$ along with the interaction effect of (D, L) .

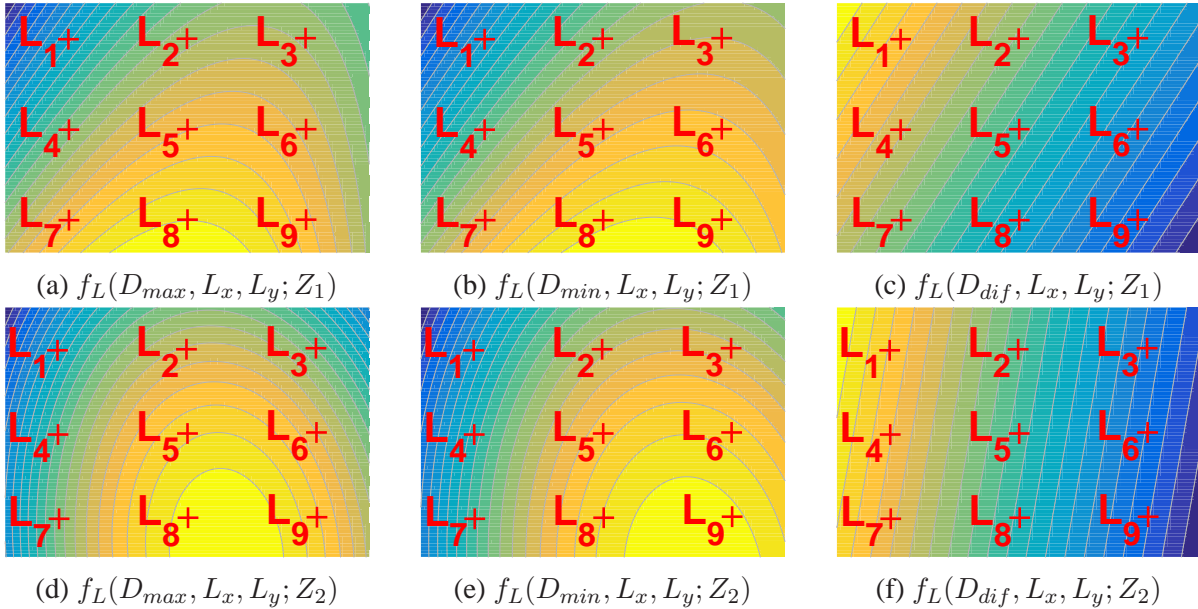


Fig 14: Mean lateral resolution with respect to location L under the conditions of Z at $MTF10$. Three heatmaps in each condition are shown: lateral resolutions (a) at D_{max} when Z_1 , where D_{max} is the distance that gives the highest mean lateral resolution, (b) at D_{min} when Z_1 , where D_{min} is the distance that gives the lowest mean lateral resolution, (c) at D_{dif} when Z_1 , where $f_L(D_{dif}, L_x, L_y; Z_1) = f_L(D_{max}, L_x, L_y; Z_1) - f_L(D_{min}, L_x, L_y; Z_1)$, (d) at D_{max} when Z_2 , (e) at D_{min} when Z_2 , and (f) at D_{dif} when Z_2 . The brighter the color, the higher the lateral resolution. Note that the color schemes in the plots are independent of each other in order to compare the relative lateral resolution according to L in an image.

Table 4: Minimum resolvable distance (d_L) of the light field cameras [mm] at MTF_{10} .

Minimum d_L		Maximum d_L	
Condition	Value	Condition	Value
(Z_1, D_5, L_8)	0.4709	(Z_1, D_1, L_1)	0.4985
(Z_2, D_6, L_8)	0.3220	(Z_2, D_{15}, L_1)	0.3465

Replicate The three replicates of the experiment did not exhibit a significant difference.

Distance The lateral resolution depends on the distance between the camera and the resolution target plate. Particularly when Z_2 , the lateral resolution tends to degrade considerably as the distance increases.

Camera Two light field cameras used in the study did not show a significant difference in lateral resolution. This implies that a consistent lateral resolution is expected from different units of the light field camera model tested in this study.

Zoom A higher lateral resolution is obtained at a higher level of zoom (Z_2) than at a lower level of zoom (Z_1). When a higher zoom level is used, the lateral resolution is also affected by the distance as the interaction between D and Z becomes significant.

Location The lateral resolution depends on the location of a scene object in the camera’s field-of-view. The central region provides a higher resolution than the peripheral region.

Illumination Changes in illumination condition did not affect the lateral resolution of the cameras with automatic camera settings for white balance and exposure mode and normalization of the images.

5 Conclusions and Future Work

Light field cameras can be an effective 3-D imaging tool for forensic investigations since they are convenient to use, portable, and affordable for most forensic laboratories. The key component

to be suitable for forensic applications is that the cameras have high accuracy in 3-D estimation and sufficient lateral and depth resolutions. In this study, we examined the lateral resolution of commercially available light field cameras. A full factorial experiment was conducted with the variables including distance between camera and object, cameras from the same model, zoom, location in the camera's field-of-view, and illumination. We observed that the average lateral resolution ranged from 1.0031 lp/mm to 1.0618 lp/mm (the minimum resolvable distance from 0.4709 mm to 0.4985 mm) when a lower zoom level was used. When a higher zoom level was used, the average lateral resolution ranged from 1.4429 lp/mm to 1.5529 lp/mm (the minimum resolvable distance from 0.3220 mm to 0.3465 mm).

The method for lateral resolution evaluation presented in this paper can be further enhanced for more accurate measurement as follows:

- The resolution target plate needs to include reference grayscale patches for image normalization.
- A test for the cameras to prevent saturation needs to be done before data collection.
- Ideally, the imaging sensor of the camera and the resolution target plate must be parallel to each other. A method to either ensure this property or measure the accurate pan and tilt angles of the resolution target plate relative to the camera axis and compensate data for the unwanted pan and tilt angles afterwards is needed during the data collection.

We will continue the study along the following directions:

- Different decoding algorithms can be used to convert raw light field images to 4-D light field data. This way, the impact of decoding algorithms on the camera resolutions can be evaluated.

- The angular variation of the lateral resolution can be analyzed in 2-D MTF.
- The lateral resolution of a light field camera is expected to be greatly improved by using a super-resolution^{29,30} or refocusing algorithm,⁶ or focused light field camera.¹⁵ This will provide the upper-limit of the resolutions expected from light field cameras.
- We will evaluate the depth resolution of the same light field cameras.

The analysis results of the lateral resolution evaluation of the light field cameras are available online with an interactive user interface at: <https://isg.nist.gov/deepzoomweb/resources/lytroEvaluations/index.html>.

Acknowledgments

The authors would like to thank the National Institute of Standards and Technology (NIST) Forensic Science Research program and NIST Computational Science in Metrology (CS-MET; <https://www.nist.gov/itl/ssd/computational-science-metrology>) for the support for this work. Also, we would like to thank William F. Guthrie, John Lu, and Hari Iyer in Statistical Engineering Division at NIST for valuable discussions, and Vincent Chiriaco in NIST printing office for preparing the resolution targets. Commercial products are identified in this document in order to specify the experimental procedure adequately. Such identification is not intended to imply recommendation or endorsement by the National Institute of Standards and Technology, nor is it intended to imply that the products identified are necessarily the best available for the purpose.

References

- 1 M. G. Lippmann, “Integral photography,” *Academy of Sciences* , 446–451 (1908).

- 2 E. H. Adelson and J. Y. A. Wang, “Single lens stereo with a plenoptic camera,” *IEEE Transactions on Pattern Analysis and Machine Intelligence* **14**(2), 99–106 (1992). [doi:10.1109/34.121783].
- 3 V. Vaish, B. Wilburn, N. Joshi, *et al.*, “Using plane + parallax for calibrating dense camera arrays,” in *IEEE Conference on Computer Vision and Pattern Recognition*, **1**, I–2–I–9 (2004). [doi:10.1109/CVPR.2004.1315006].
- 4 T. Georgeiv, K. C. Zheng, B. Curless, *et al.*, “Spatio-angular resolution tradeoffs in integral photography,” in *Eurographics Conference on Rendering Techniques*, 263–272 (2006). [doi:10.2312/EGWR/EGSR06/263-272].
- 5 R. Ng, M. Levoy, M. Bredif, *et al.*, “Light field photography with a hand-held plenoptic camera,” Tech. Rep. CTST 2005–02, Stanford University (2005).
- 6 A. Isaksen, L. McMillan, and S. J. Gortler, “Dynamically reparameterized light fields,” in *SIGGRAPH*, 297–306 (2000). [doi:10.1145/344779.344929].
- 7 K. Honauer, O. Johannsen, D. Kondermann, *et al.*, “A dataset and evaluation methodology for depth estimation on 4D light fields,” in *Asian Conference on Computer Vision*, (2016).
- 8 ISO 12233, “Photography – Electronic still picture imaging – Resolution and spatial frequency responses,” (2017).
- 9 P. D. Burns, “Slanted-edge MTF for digital camera and scanner analysis,” in *Society for Imaging Science and Technology: Image Processing, Image Quality, Image Capture, Systems Conference*, 135–138 (2000).
- 10 C. Loebich, D. Wueller, B. Klingen, *et al.*, “Digital camera resolution measurement using sinusoidal Siemens stars,” in *Proceedings of SPIE 6502, Digital Photography III*, (2007).

- 11 D. Williams, D. Wueller, K. Matherson, *et al.*, “A pilot study of digital camera resolution metrology protocols proposed under ISO 12233, edition 2,” in *Proceedings of SPIE 6808, Image Quality and System Performance V*, (2008). [doi:10.1117/12.768204].
- 12 Imatest, “Standard eSFR ISO chart.” http://www.imatest.com/wp-content/uploads/2014/06/new_ISO-12233_plain_vanilla.png. [Date accessed: May 7, 2018].
- 13 Siemens Star Focus Chart. <https://photographylife.com/wp-content/uploads/2012/07/Siemens-Star-Focus-Chart.pdf>. [Date accessed: May 7, 2018].
- 14 D. Firmenich, L. Baboulaz, and S. Süsstrunk, “A practical method for measuring the spatial frequency response of light field cameras,” in *IEEE International Conference on Image Processing*, 5776–5780 (2014). [doi:10.1109/ICIP.2014.7026168].
- 15 A. Lumsdaine and T. Georgiev, “The focused plenoptic camera,” in *IEEE International Conference on Computational Photography*, 1–8 (2009). [doi:10.1109/ICCPHOT.2009.5559008].
- 16 Q. Fu, Z. Zhou, Y. Yuan, *et al.*, “Image quality evaluation of light field photography,” in *Proceedings of SPIE 7867, Image Quality and System Performance VIII*, (2011). [doi:10.1117/12.872486].
- 17 M. Damghanian, R. Olsson, M. Sjöström, *et al.*, “Spatial resolution in a multi-focus plenoptic camera,” in *IEEE International Conference on Image Processing*, 1932–1936 (2014). [doi:10.1109/ICIP.2014.7025387].
- 18 Raytrix GmbH. <http://www.raytrix.de/>. [Date accessed: May 7, 2018].

- 19 Lytro, Inc. <https://www.lytro.com/>. [Date accessed: March 26, 2018].
- 20 G. E. P. Box, J. S. Hunter, and W. G. Hunter, *Statistics for Experimenters: Design, Innovation, and Discovery*, Wiley, 2nd ed. (2005).
- 21 J. A. Speir, N. Richetelli, M. Fagert, *et al.*, “Quantifying randomly acquired characteristics on outsoles in terms of shape and position,” *Forensic Science International* **266**, 399–411 (2016). [doi:10.1016/j.forsciint.2016.06.012].
- 22 B. Kong, J. Supancic, D. Ramanan, *et al.*, “Cross-domain forensic shoeprint matching,” in *British Machine Vision Conference*, (2017).
- 23 Ricoh Pro C7100. <https://www.ricoh-usa.com/en/products/commercial-industrial-printing/cutsheet/pro-c7100-c7100x-series>. [Date accessed: May 7, 2018].
- 24 R. S. of International Telecommunication Union, “Studio encoding parameters of digital television for standard 4:3 and wide-screen 16:9 aspect ratios,” in *Recommendation ITU-R BT.601-7*, (2011).
- 25 N. Otsu, “A threshold selection method from gray-level histograms,” *IEEE Transactions on Systems, Man, and Cybernetics* **9**(1), 62–66 (1979). [doi:10.1109/TSMC.1979.4310076].
- 26 I. D. Coope, “Circle fitting by linear and nonlinear least squares,” *Journal of Optimization Theory and Applications* **76**(2), 381–388 (1993). [doi:10.1007/BF00939613].
- 27 LabVIEW. <http://www.ni.com/en-us/shop/labview.html>, note = [Date accessed: July 12, 2018].
- 28 Konica Minolta CS-100 Chroma Meter. <https://sensing.konicaminolta.us/>

[products/cs-100a-luminance-and-color-meter/](#). [Date accessed: July 16, 2018].

- 29 T. E. Bishop and P. Favaro, “The light field camera: Extended depth of field, aliasing, and superresolution,” *IEEE Transactions on Pattern Analysis and Machine Intelligence* **34**(5), 972–986 (2012). [doi:10.1109/TPAMI.2011.168].
- 30 S. Wanner and B. Goldluecke, “Variational light field analysis for disparity estimation and super-resolution,” *IEEE Transactions on Pattern Analysis and Machine Intelligence* **35**(3), 606–619 (2014). [doi:10.1109/TPAMI.2013.147].

Sowon J. Yoon received her PhD degree in computer science and engineering from Michigan State University in 2014, and the BS and MS degrees in electrical and electronic engineering from Yonsei University, Seoul, South Korea, in 2006 and 2008, respectively. She is a scientific research specialist at Dakota Consulting Inc. associated with NIST. Her research interests include image processing, pattern recognition, and computer vision in the areas of biometrics, bioimage analysis, and 3-D computer vision.

Peter Bajcsy received his PhD degree in electrical and computer engineering in 1997 from the University of Illinois at Urbana-Champaign (UIUC). He worked for Cognex, Demaco/SAIC, and NCSA/UIUC before joining NIST in 2011. His area of research is large-scale image-based analyses and syntheses using mathematical, statistical, and computational models while leveraging computer science fields. such as image processing, machine learning, computer vision, and pattern recognition. For more information, see <https://www.nist.gov/people/peter-bajcsy>.

Maritoni Litorja received her PhD degree in physical chemistry from Northwestern University in

1996. After a postdoctoral stint at Argonne National Laboratory, she came to NIST as a NRC/NIST postdoctoral fellow in 1999 and has been at NIST ever since. Her work is on the dissemination of the SI in optical technologies for metrology of dimensions (length) and substance quantification. She works on optical radiometry and imaging measurement science applications in diverse areas encompassing biomedicine, forensics, and climate research.

James J. Filliben received his PhD degree in statistics from Princeton University in 1969. He is a member of Statistical Engineering Division at NIST since 1969. He is the author of *Dataplot: Statistical Graphics and Modeling System* (1978), and a fellow of American Statistical Association (ASA). He received the ASA Youden Award and a number of Department of Commerce Medals. His research interests include statistical graphics, design of experiments, distributional modeling, computational modeling/verification/validation, and uncertainty/sensitivity analysis.